AIAA JOURNAL
Vol. 33, No. 12, December 1995

Large Eddy Simulation of Reacting Flows Applied to Bluff Body Stabilized Flames

C. Fureby* and S.-I. Möller†
Lund Institute of Technology, S-221 00 Lund, Sweden

The objective of this paper is to present a large eddy simulation model for chemically reacting flows. The large eddy simulation model, founded on a physical model based on modern continuum mechanics, includes a complete treatment of the subgrid stresses and fluxes including both backscatter and diffusion. To investigate the predictive capabilities of the large eddy simulation model, numerical simulations of a configuration corresponding to a rig consisting of a rectilinear channel with a triangular-shaped bluff body have been performed. Both nonreacting and reacting flows have been examined under a variety of operating conditions. This paper focuses on the reacting case, which is characterized as lean and premixed. The simulation results are compared to experimental measurements of temperature, constituent mass fraction, and velocity fields in the test rig. The results indicate that the large eddy simulation technique works well and mimics most of the significant flow features, including the typical unsteady flow structures. The results from the large eddy simulations are furthermore used to investigate the mechanisms responsible for the typical flowfield in a bluff body stabilized flame.

Nomenclature

A_j	= pre-exponential factor
$\boldsymbol{b}$	= specific body force
$\boldsymbol{C}, \boldsymbol{c}_A, \boldsymbol{c}_h$	= cross stress tensor and flux vectors
E_j	= activation energy
$\boldsymbol{h}$	= heat conduction vector, κ grad θ
h_{Af}	= constituent formation enthalpy
$\boldsymbol{I}$	= identity tensor
k	= Stefan–Boltzmann constant
$\boldsymbol{L}, \boldsymbol{l}_A, \boldsymbol{l}_h$	= Leonard stress tensor and flux vectors
M_A	= molar mass
$\hat{m}_A$	= mass supply term
R	= universal gas constant
$\boldsymbol{R}, \boldsymbol{r}_A, \boldsymbol{r}_h$	= Reynolds stress tensor and flux vectors
w_j	= reaction rate of reaction j
$\dot{\boldsymbol{x}}$	= barycentric velocity
Y_A	= mass fraction
θ	= temperature
ι	= radiation intensity
κ	= conductivity, $\kappa(\rho, \theta)$
κ_A	= mass diffusivity, $\kappa_A(\rho, \theta)$
ρ	= density
Ξ_A	= constituent symbol
σ	= sum of net radiation and power generated by specific body forces and mass diffusion
$\tilde{\sigma}$	= filtered source term for radiative heat transfer in energy equation
σ_A	= absorption coefficient
$\upsilon^R_{Aj}, \upsilon^P_{Aj}$	= stoichiometric coefficients for reactants and products, respectively

Introduction

DIRECT numerical simulation (DNS) of turbulent flows at high Reynolds (Re) number, encountered in many problems of technological importance, is almost impossible since the physical and chemical processes occur at a wide range of time and space scales. Consequently, the solutions to such problems must so far be based on some form of modeling. Traditional methods such as Reynolds average simulations (RAS) have had only limited success since the large eddies, containing most of the energy, are strongly dependent on the geometry of the flow considered; the small eddies are more universal in character and serve mainly as a source for dissipation. Following Deardorff,[1] it can be argued that better understanding of turbulent flows can be achieved if the motions of the large eddies are simulated whereas the effect of the small eddies on the large eddies is modeled. During the past decades, considerable progress has been made in large eddy simulations (LES) of isochoric flows.[2,3] Despite the intensive research devoted to LES of isochoric flows, it appears that only few LESs, of anisochoric flows[4–6] or of reacting mixtures[7–9] have been attempted.

During the past 25 years there has been increased interest in more accurate descriptions of combustion in order to, e.g., help improving thermal efficiency with minimal noise and pollutant formation in combustion applications. Simulating combustion systems has its own particular problems because of the strong interaction between the energy release from chemical reactions and the dynamics of fluid motion. The energy released generates gradients in temperature, pressure, and density. These gradients influence the transport of mass, momentum, and energy in the system. On a large scale, these gradients generate vorticity or affect the diffusion of mass and energy. On a small scale, they are the origin of turbulence, which affects microscopic mixing and burning rates. A proper description of the strong interplay between chemistry and fluid dynamics is, therefore, important when investigating chemically reacting mixtures.

The objective of this study is to extend previous efforts[6,8] in developing a LES model for turbulent chemically reacting mixtures. In the present investigation we will focus on evaluating the predictive capabilities of the LES model by collating results from three-dimensional numerical simulations with experimental data. Furthermore, following and extending the ideas outlined in Ref. 6, the basic morphology of the flow will be discussed in order to obtain as much relevant information as possible regarding the physical processes involved. The main aim of the investigations presented in this work and in Ref. 6 is to construct a firm basis for investigating various subgrid scale (SGS) models more in detail, see Refs. 10 and 11 for further details.

Physical Model for Chemically Reacting Flows

A chemically reacting flow can be treated as a mixture assumed to consist of N bodies that are allowed to occupy common portions of physical space. By adopting the postulates of Truesdell[12] balance

Received Nov. 29, 1994; revision received April 24, 1995; accepted for publication May 22, 1995.

*Department of Physics, Division of Combustion Physics, Box 118; currently Department of Mechanical Engineering, Thermo-Fluids Section, Imperial College, Exhibition Road, SW7 2AZ London, England, United Kingdom.

†Graduate Student, Department of Mathematical Physics and Mechanics, Division of Mechanics, Box 118.

equations for mass, momentum, rotational momentum, and energy, including supply terms accounting for the interactions between the constituents, can be formulated. Furthermore, to close the set of balance equations, constitutive equations must be formulated, see Ref. 13. Since the mixture model must be simple enough to solve practical problems, but still general enough to mimic the physical behavior, some simplifications must be adopted: 1) The mixture has only one temperature. 2) The stress tensor of the mixture is symmetric. 3) The fluid is assumed to be linearly viscous with Fourier heat conduction. Thus,

$$\partial_t(\rho Y_A) + \operatorname{div}(\rho Y_A \dot{\boldsymbol{x}}) = \operatorname{div}\boldsymbol{d}_A + \hat{m}_A, \qquad A = 1, \ldots, N \tag{1a}$$

$$\partial_t(\rho) + \operatorname{div}(\rho \dot{\boldsymbol{x}}) = 0 \tag{1b}$$

$$\partial_t(\rho \dot{\boldsymbol{x}}) + \operatorname{div}(\rho \dot{\boldsymbol{x}} \otimes \dot{\boldsymbol{x}}) = -\operatorname{grad} p + \operatorname{div}\boldsymbol{S} + \rho \boldsymbol{b} \tag{1c}$$

$$\partial_t(\rho h) + \operatorname{div}(\rho h \dot{\boldsymbol{x}}) = \dot{p} + \boldsymbol{S} \cdot \boldsymbol{D} + \operatorname{div}\boldsymbol{h} + \rho\sigma \tag{1d}$$

where $\boldsymbol{d}_A = -\rho Y_A \boldsymbol{u}_A = \kappa_A \operatorname{grad} Y_A$ are the mass diffusion vectors, $p = \rho R\theta \sum (Y_A / M_A)$ is the thermodynamic pressure, $\boldsymbol{S} = \lambda \operatorname{tr}\boldsymbol{D}\boldsymbol{I} + 2\mu\boldsymbol{D}$ is the extra stress tensor, $\lambda = \lambda(\rho, \theta)$ and $\mu = \mu(\rho, \theta)$ are the coefficients of viscosity. $\boldsymbol{D} = \frac{1}{2}(\boldsymbol{L} + \boldsymbol{L}^T)$ is the rate of strain tensor where $\boldsymbol{L} = \operatorname{grad}\dot{\boldsymbol{x}}$,

$$h = \sum \left[Y_A \left(h_{Af} + \int_\theta C_{PA}\, \mathrm{d}\theta + \rho \boldsymbol{u}_A^2 \right) \right]$$

is the specific enthalpy, where $C_{PA} = C_{PA}(\theta)$ the specific heats,

$$\boldsymbol{S} \cdot \boldsymbol{D} = \lambda(\operatorname{div}\dot{\boldsymbol{x}})^2 + 2\mu \boldsymbol{D}^2$$

is the dissipation function.

Large Eddy Simulation Model

In LES it is assumed that the flow can be decomposed into two parts. For the flow of a compressible fluid, the density weighted decomposition, given by $\rho = \bar{\rho} + \rho'$ and $\phi = \tilde{\phi} + \phi''$ where $\overline{\rho\phi} = \bar{\rho}\tilde{\phi}$, is normally utilized. The first part, described by $\{\bar{\rho}, \tilde{\phi}\}$, contains the large-scale eddies depending on the geometry of the flow domain in terms of the boundary conditions. The second part, described by $\{\rho', \phi''\}$, contains the small-scale eddies, whose effects on the large-scale eddies are to be described by separate models. To obtain the governing equations for the large-scale motion the balance equations (1) are spatially filtered by the convolution,

$$\bar{\phi} = \int_D G(\boldsymbol{x} - \boldsymbol{z}, \Delta)\phi(\boldsymbol{z}, t)\, \mathrm{d}^3\boldsymbol{z} \tag{2}$$

where the kernel $G = G(\boldsymbol{x} - \boldsymbol{z})$ is the filter function and the integration is over the entire computational domain D. Applying the filter operation to an arbitrary variable means that the amplitude of the high wave number spatial Fourier components are reduced, thus decreasing the high demands for spatial resolution. The filter function must satisfy the following criteria: Firstly, G must be normalized, $\int_D G(\boldsymbol{x} - \boldsymbol{z})\, \mathrm{d}^3\boldsymbol{z} = 1$. Secondly, in the limit as the distance between adjacent grid points decrease, G becomes a Dirac function; thus,

$$\lim_{\Delta \to 0} \int_D G(\boldsymbol{x} - \boldsymbol{z})\phi(\boldsymbol{z}, t)\, \mathrm{d}^3\boldsymbol{z} = \phi(\boldsymbol{x}, t)$$

Finally, G should be taken as an infinitely differentiable generalized function (i.e., a distribution) of bounded support in a bounded region on $G = G(\boldsymbol{x} - \boldsymbol{z}) \in D$ where $D = \{\psi \in C^n(R^3),\ \psi$ has compact support$\}$. Hence,

$$\begin{aligned}
&\partial_t(\bar{\rho}\tilde{Y}_A) + \operatorname{div}(\bar{\rho}\tilde{Y}_A\tilde{\dot{\boldsymbol{x}}}) = \operatorname{div}(\bar{\boldsymbol{d}}_A - \boldsymbol{b}_A) + \bar{\hat{m}}_A \\
&\partial_t(\bar{\rho}) + \operatorname{div}(\bar{\rho}\tilde{\dot{\boldsymbol{x}}}) = 0 \\
&\partial_t(\bar{\rho}\tilde{\dot{\boldsymbol{x}}}) + \operatorname{div}(\bar{\rho}\tilde{\dot{\boldsymbol{x}}} \otimes \tilde{\dot{\boldsymbol{x}}}) = -\operatorname{grad}\bar{p} + \operatorname{div}(\bar{\boldsymbol{S}} - \boldsymbol{B}) + \bar{\rho}\tilde{\boldsymbol{b}} \\
&\partial_t(\bar{\rho}\tilde{h}) + \operatorname{div}(\bar{\rho}\tilde{h}\tilde{\dot{\boldsymbol{x}}}) = \bar{\dot{p}} + \overline{\boldsymbol{S} \cdot \boldsymbol{D}} + \bar{\rho}\tilde{\sigma} + \operatorname{div}(\bar{\boldsymbol{h}} - \boldsymbol{b}_h)
\end{aligned} \tag{3}$$

where we have introduced the density weighted SGS stresses and fluxes defined by

$$\begin{aligned}
\boldsymbol{B} &= \bar{\rho}(\widetilde{\dot{\boldsymbol{x}} \otimes \dot{\boldsymbol{x}}} - \tilde{\dot{\boldsymbol{x}}} \otimes \tilde{\dot{\boldsymbol{x}}}) = \bar{\rho}(\widetilde{\tilde{\dot{\boldsymbol{x}}} \otimes \tilde{\dot{\boldsymbol{x}}}} - \tilde{\dot{\boldsymbol{x}}} \otimes \tilde{\dot{\boldsymbol{x}}}) \\
&\quad + \bar{\rho}(\widetilde{\tilde{\dot{\boldsymbol{x}}} \otimes \dot{\boldsymbol{x}}''} + \widetilde{\dot{\boldsymbol{x}}'' \otimes \tilde{\dot{\boldsymbol{x}}}}) + \bar{\rho}(\widetilde{\dot{\boldsymbol{x}}'' \otimes \dot{\boldsymbol{x}}''}) = \boldsymbol{L} + \boldsymbol{C} + \boldsymbol{R} \\
\boldsymbol{b}_h &= \bar{\rho}(\widetilde{\dot{\boldsymbol{x}}h} - \tilde{\dot{\boldsymbol{x}}}\tilde{h}) = \bar{\rho}(\widetilde{\tilde{\dot{\boldsymbol{x}}}\tilde{h}} - \tilde{\dot{\boldsymbol{x}}}\tilde{h}) + \bar{\rho}(\widetilde{\tilde{\dot{\boldsymbol{x}}}h''} + \widetilde{\dot{\boldsymbol{x}}''\tilde{h}}) \\
&\quad + \bar{\rho}(\widetilde{h''\dot{\boldsymbol{x}}''}) = \boldsymbol{l}_h + \boldsymbol{c}_h + \boldsymbol{r}_h \\
\boldsymbol{b}_A &= \bar{\rho}(\widetilde{\dot{\boldsymbol{x}}Y_A} - \tilde{\dot{\boldsymbol{x}}}\tilde{Y}_A) = \bar{\rho}(\widetilde{\tilde{\dot{\boldsymbol{x}}}\tilde{Y}_A} - \tilde{\dot{\boldsymbol{x}}}\tilde{Y}_A) + \bar{\rho}(\widetilde{\tilde{\dot{\boldsymbol{x}}}Y_A''} + \widetilde{\dot{\boldsymbol{x}}''\tilde{Y}_A}) \\
&\quad + \bar{\rho}(\widetilde{Y_A''\dot{\boldsymbol{x}}''}) = \boldsymbol{l}_A + \boldsymbol{c}_A + \boldsymbol{r}_A
\end{aligned} \tag{4}$$

The terms appearing in the filtered set of balance equations (4) can be divided into four categories: 1) $\bar{\rho}, \tilde{Y}_A, \tilde{\dot{\boldsymbol{x}}}$, and $\tilde{h}$; 2) $\boldsymbol{R}, \boldsymbol{r}_A$, and $\boldsymbol{r}_h$; 3) $\boldsymbol{L}, \boldsymbol{l}_A, \boldsymbol{l}_h, \boldsymbol{C}, \boldsymbol{c}_A$, and $\boldsymbol{c}_h$; and 4) $\bar{\boldsymbol{d}}_A, \bar{\hat{m}}_A, \bar{\boldsymbol{S}}, \bar{\boldsymbol{b}}, \bar{p}, \overline{\boldsymbol{S} \cdot \boldsymbol{D}}, \bar{\boldsymbol{h}}$ and $\bar{\sigma}$. The terms in group 1 represent the grid scale (GS) components of the dependent variables, and their evaluation is the main goal of LES. The terms in group 2, the Reynolds terms, represent the correlations of SGS fluctuations and require modeling; their main effect is dissipation or outscatter. The terms in group 3 are particular only to LES and do not appear in RAS. Leslie and Quarini[14] emphasize that the major effect of the Leonard terms is redistribution among the GSs, whereas the major effect of the cross terms is backscatter or transfer from SGSs back to the GSs. The Leonard terms can be calculated explicitly without additional modeling, whereas the cross terms have to be modeled. The terms in group 4 are nonlinear and can not be evaluated without additional assumptions. Assuming that the SGS fluctuations in the thermal conductivity, the mass diffusivities, and in the viscosities can be neglected yields the following approximate expressions:

$$\begin{aligned}
\bar{\boldsymbol{d}}_A &= \overline{\kappa_A \operatorname{grad} Y_A} \approx \bar{\kappa}_A \operatorname{grad}\tilde{Y}_A \\
\bar{\boldsymbol{S}} &= \overline{(\lambda \operatorname{tr}\boldsymbol{D})\boldsymbol{I} + 2\mu\boldsymbol{D}} \approx (\bar{\lambda} \operatorname{tr}\tilde{\boldsymbol{D}})\boldsymbol{I} + 2\bar{\mu}\tilde{\boldsymbol{D}} \\
\bar{\boldsymbol{h}} &= \overline{\kappa \operatorname{grad}\theta} \approx \bar{\kappa} \operatorname{grad}\tilde{\theta}
\end{aligned} \tag{5}$$

where $\bar{\kappa}_A = \kappa_A(\bar{\rho}, \tilde{\theta})$, $\bar{\lambda} = \lambda(\bar{\rho}, \tilde{\theta})$, $\bar{\mu} = \mu(\bar{\rho}, \tilde{\theta})$, and $\bar{\kappa} = \kappa(\bar{\rho}, \tilde{\theta})$. The filtered dissipation function and the filtered material time derivative of pressure can be calculated according to

$$\overline{\boldsymbol{S} \cdot \boldsymbol{D}} = \overline{(\bar{\boldsymbol{S}} + \boldsymbol{S}') \cdot (\tilde{\boldsymbol{D}} + \boldsymbol{D}'')} = \overline{\bar{\boldsymbol{S}} \cdot \tilde{\boldsymbol{D}}} + \overline{\bar{\boldsymbol{S}} \cdot \boldsymbol{D}''} + \overline{\boldsymbol{S}' \cdot \tilde{\boldsymbol{D}}} + \overline{\boldsymbol{S}' \cdot \boldsymbol{D}''} \tag{6a}$$

$$\begin{aligned}
\bar{\dot{p}} &= \overline{\partial_t(\rho) + \dot{\boldsymbol{x}} \cdot \operatorname{grad} p} = \partial_t(\bar{\rho}) + \overline{\tilde{\dot{\boldsymbol{x}}} \cdot \operatorname{grad}\bar{p}} \\
&\quad + \overline{\tilde{\dot{\boldsymbol{x}}} \cdot \operatorname{grad} p'} + \overline{\dot{\boldsymbol{x}}'' \cdot \operatorname{grad}\bar{p}} + \overline{\dot{\boldsymbol{x}}'' \cdot \operatorname{grad} p'}
\end{aligned} \tag{6b}$$

The dissipation function (6a) and the substantial time derivative of pressure (6b) contain additional terms that have to be prescribed before a complete set of equations are found. For this initial study the terms containing fluctuating components are neglected. The error introduced by this approximation is negligible in flows with low heat release since these terms are small in comparison with the specific enthalpy variation of the fluid; however, in flows with significant heat release, SGS pressure gradients can be fairly large in regions close to, e.g., the flamefront. Recently, work has been initiated to investigate the importance of the SGS terms in Eqs. (6) utilizing DNS of both nonreacting and reacting mixtures with and without heat release.

Analysis of DNS data, e.g., Ref. 15, has shown that backscatter can occur over significant parts in the flow domain. Furthermore, other studies[16,17] have shown that the dissipation and backscatter are two distinct processes and, therefore, should be treated separately. The aforementioned investigations motivate us to model the individual SGS terms separately.

The Leonard terms $\{\boldsymbol{L}, \boldsymbol{l}_h, \boldsymbol{l}_A\}$ are in this study explicitly calculated since they are only functionals of the GS components of the dependent variables. Extending the analysis of Leonard,[18] using Taylor series expansions of the GS components, it is found that the

leading-order term in each of the Taylor series expansions of the Leonard terms is proportional to Δ^2 where Δ is the filter width. This implies that at least third-order accurate numerical methods are needed in order to calculate the individual terms constituting the SGS stresses and fluxes.

The cross terms $\{\boldsymbol{C}, \boldsymbol{c}_h, \boldsymbol{c}_A\}$ are functionals of both the GS and the SGS components of the dependent variables and must, consequently, be modeled. Currently, a number of models based on phenomenological ideas or assumptions for the cross terms are available, among these, the linear combination model[19] and a model based on stochastic backscatter driven by a random force[20] are among the most well known. The linear combination model is founded on the assumption that the interactions between the GS and SGS components of the flowfield takes place mainly between the segments of each of the fields that are most alike. The primary interactions are, consequently, between the smallest scales of the GS components and the largest scales of the SGS components. To include this effect, the small-scale component of the GS components must be defined. One interesting approach is suggested by Bardina et al.[19] who observed that repeated filtering of a scalar valued field produces a GS field, which is still richer in the large scales. In this study we follow Speziale et al.[5] and adopt a compressible analog to the linear combination model.

The Reynolds terms $\{\boldsymbol{R}, \boldsymbol{r}_h, \boldsymbol{r}_A\}$ are only functionals of the SGS components and must, therefore, also be modeled. The most popular models for the Reynolds terms are based on the assumptions: $\boldsymbol{R} = \frac{2}{3}\bar{\rho}q_R\boldsymbol{I} + 2\mu_R\tilde{\boldsymbol{D}}_D$, $\boldsymbol{r}_h = \kappa_{rh}\operatorname{grad}\tilde{h}$, and $\boldsymbol{r}_A = \kappa_{rA}\operatorname{grad}\tilde{Y}_A$, where $\tilde{\boldsymbol{D}}_D$ is the deviator of $\tilde{\boldsymbol{D}}$; q_R is the specific SGS kinetic energy related to $\boldsymbol{R}$; and μ_R, κ_{rh}, and κ_{rA} are the eddy viscosity and diffusivity coefficients that can be related to the characteristic time and length scales $\tau_{\text{sgs}} = c_T\|\tilde{\boldsymbol{D}}\|^{-1}$ and $\lambda_{\text{sgs}} = c_L^{1/2}\Delta$, respectively, where $\|\tilde{\boldsymbol{D}}\|$ is the Frobenius norm of $\tilde{\boldsymbol{D}}$, by traditional dimensional arguments.

Combining the separate contributions constituting the total SGS stresses and fluxes we obtain the following expression for the total SGS stress tensor and flux vectors:

$$\begin{aligned}
\boldsymbol{B} &\approx \bar{\rho}(\widetilde{\tilde{\boldsymbol{x}}\otimes\tilde{\boldsymbol{x}}} - \tilde{\tilde{\boldsymbol{x}}}\otimes\tilde{\tilde{\boldsymbol{x}}}) + \tfrac{2}{3}c_I\bar{\rho}\Delta^2\|\tilde{\boldsymbol{D}}\|^2\boldsymbol{I} - 2c_D\bar{\rho}\Delta^2\|\tilde{\boldsymbol{D}}\|\tilde{\boldsymbol{D}}_D \\
\boldsymbol{b}_h &\approx \bar{\rho}(\widetilde{\tilde{\boldsymbol{x}}\tilde{h}} - \tilde{\tilde{\boldsymbol{x}}}\tilde{\tilde{h}}) - 2c_H\bar{\rho}\Delta^2\|\tilde{\boldsymbol{D}}\|\operatorname{grad}\tilde{h} \qquad (7) \\
\boldsymbol{b}_A &\approx \bar{\rho}(\widetilde{\tilde{\boldsymbol{x}}\tilde{Y}_A} - \tilde{\tilde{\boldsymbol{x}}}\tilde{\tilde{Y}}_A) - 2c_A\bar{\rho}\Delta^2\|\tilde{\boldsymbol{D}}\|\operatorname{grad}\tilde{Y}_A
\end{aligned}$$

where $c_I = c_L/c_T^2$, $c_D = c_L/c_T$, $c_H = \alpha(c_L/c_T)$ and, finally, $c_A = \beta(c_L/c_T)$ are dimensionless constants that have to be separately evaluated.

What remains to be specified is a relation between the filter width Δ and the local geometry on the grid. For a nonuniform grid, it is not obvious how to determine the resolved length scale. Several measures have, however, been proposed, e.g., Ref. 1. In this study we have used a box filter and assumed that $\Delta = \sqrt{(\Sigma(\Delta x_i)^2)}$ in which Δx_i is the local grid spacing in the ith direction.

Global Combustion Modeling

To obtain expressions for the mass supply terms $\hat{m}_A$ appearing in the balance equations (1d) accounting for production and destruction of each constituent due to each chemical reaction step, we consider a reaction mechanism involving N constituents and M reaction steps of the form

$$\Sigma_A \upsilon_{Aj}^R \Xi_A \rightarrow \Sigma_A \upsilon_{Aj}^P \Xi_A, \qquad A \in [1,\ldots,N], \qquad j \in [1,\ldots,M] \qquad (8)$$

where k_j are the rate constants for the reaction step j, normally expressed in Arrhenius form, i.e., $k_j = A_j\exp(-E_j/R\theta)$. For constituent A the contributions of all reactions may be expressed compactly according to

$$\begin{aligned}
\hat{m}_A &= M_A\Sigma_{j=1}^M\left(\upsilon_{Aj}^P - \upsilon_{Aj}^R\right)w_j \\
&= M_A\Sigma_{j=1}^M\left(\upsilon_{Aj}^P - \upsilon_{Aj}^R\right)\rho^{\Sigma_{A=1}^M s_{Aj}^R}k_j\Pi_{A=1}^N Y_A^{s_{Aj}^R} \qquad (9)
\end{aligned}$$

where the s_{Aj} are the stoichiometric coefficients, if reaction step j is a fundamental reaction step, else they are empirically determined numbers. Since the mass supply terms $\hat{m}_A$ are nonlinear functions of temperature, density, and mass fractions, the determination of the filtered mass supply terms $\bar{\hat{m}}_A$, or more precisely the filtered reaction rates $\bar{w}_j$, results in complex expressions involving terms accounting for the alteration of the reaction rates as given by the product of GS and SGS components of temperature, density, and mass fractions. Subsequently, the local rate of reaction can be significantly influenced by SGS phenomena.

Chemical reactions are assumed to take place when reactants are mixed on a molecular level having sufficiently high temperature for the reaction to start. Experiments[21,22] suggest that the processes occurring at the SGS level are important for molecular mixing and energy dissipation. These processes are also found to be intermittent or concentrated in isolated regions denoted fine structures. The intermittency can, according to Ref. 23, be quantified in terms of the volume fraction γ of the fine structures. From the energy cascade process, the characteristic velocity and length scales are found to be $u^* = (\frac{5}{16}\xi^{-2})^{1/4}(\nu\varepsilon)^{1/4}$ and $\lambda^* = (125\xi^2)^{1/4}(\nu^3/\varepsilon)^{1/4}$, respectively. Consequently, the expression for the volume fraction is $\gamma = \lambda^*/\lambda_{\text{sgs}} = (125\xi^2)^{1/4}\lambda_{\text{sgs}}^{-1}\nu^{3/4}\varepsilon^{-1/4}$. The dissipation of specific kinetic energy can approximatively be evaluated from $\varepsilon = (k^{3/2})\Delta^{-1}$, where $k = \frac{1}{2}(\tilde{x}^2) + q_B$ is the total specific kinetic energy. The dimensionless constant ξ is associated with the energy transfer mechanism in the cascade process and can be evaluated by demanding that the SGS dissipation rate ε_{sgs} and the dissipation at the first level in the cascade process ε' are equal; hence, $\xi = 0.09$. Within the fine structures it is implicitly assumed that the reactants are mixed at a molecular scale and create the reaction space for nonuniformly distributed reactants.

The filtered mass supply terms can, thus, formally be approximated as a reciprocal sum of two time scales related to mass transfer and chemical reactions, respectively. Hence,

$$\begin{aligned}
\bar{\hat{m}}_A &= M_A\Sigma_A\left(\upsilon_{Aj}^P - \upsilon_{Aj}^R\right)\bar{w}_j \\
&= M_A\Sigma_A\left(\upsilon_{Aj}^P - \upsilon_{Aj}^R\right)\left[\left(\bar{w}_j^{\text{mass}}\right)^{-1} + \left(\bar{w}_j^{\text{chem}}\right)^{-1}\right]^{-1} \qquad (10)
\end{aligned}$$

where $\bar{w}_j^{\text{mass}}$ is the net mass transfer rate for reaction j between the fine structures and their surroundings, and $\bar{w}_j^{\text{chem}}$ is the chemical reaction rate for reaction j based on the Arrhenius rate expressions. Geometrical considerations yield that the mass flow per unit mass and time between the fine structures and the surrounding fluid can be expressed as $\dot{m} = (u^*/\lambda^*)\gamma = u^*/\lambda_{\text{sgs}} = (\frac{5}{16}\xi^{-2})^{1/4}(\varepsilon\nu)^{1/4}$. The resulting mass transfer rate for reaction j can, consequently be expressed by

$$\bar{w}_j^{\text{mass}} = \left(\bar{\rho}\tau_M^{-1}\right)\min\left\{\tilde{Y}_A\left[-\left(\upsilon_{Aj}^P - \upsilon_{Aj}^R\right)M_A\right]^{-1}\right\} \qquad (11)$$

where τ_M is a characteristic time scale for SGS mixing related to the volume fraction γ and the mass flow $\dot{m}$ according to $\tau_M = (1-\gamma)/\dot{m}$.

In this investigation we will focus on premixed combustion of hydrocarbon fuels. The oxidation of any hydrocarbon fuel $C_nH_{(2n+2)}$ consists primarily of the sequential fragmentation of the initial fuel molecule into intermediate constituents, which are ultimately converted into products usually dominated by H_2O and CO_2. Extending the description utilized in Ref. 8, the four-step global reaction mechanism of Hautmann et al.[24] is adopted here

$$C_nH_{(2n+2)} \rightarrow (n/2)C_2H_4 + (2n+1)H_2 \qquad (12a)$$

$$C_2H_4 + O_2 \rightarrow 2CO + 2H_2 \qquad (12b)$$

$$CO + \tfrac{1}{2}O_2 \rightarrow CO_2 \qquad (12c)$$

$$H_2 + \tfrac{1}{2}O_2 \rightarrow H_2O \qquad (12d)$$

where ethene (C_2H_4), in principle, represents the presence of all hydrocarbon intermediates that are formed during the oxidation process.

Additional Submodels

To describe processes such as thermal radiation and emission formation, additional submodels are needed. In this section we will present a novel approach for including thermal radiation and NO formation in the LES model earlier described. Both thermal radiation and NO formation are processes which are sensitive to local temperature variations and, therefore, the models adopted may be oversimplified; this aspect will be addressed in greater detail in a forthcoming study.

The interaction of radiation passing through a medium can be described by its absorption, scattering, and transmission. Absorption and scattering processes will reduce the intensity of a flux in a certain direction, whereas the volume element under consideration is emitting new radiation due to its composition and temperature. An energy balance for a finite control volume leads to the radiative transfer equation, which under the assumptions of grey gas and nonscattering medium is

$$\tilde{\sigma} = \sigma_a \int_{\Omega=4\pi} \iota \, d\Omega - 4\sigma_a k \tilde{\theta}^4 \tag{13}$$

In addition to the global combustion model describing the primary oxidation of the hydrocarbon fuel, a separate model for the additional NO formation has been adopted. Assuming fuel lean conditions, the NO emission is believed to come from two main sources.[25–27] The first is described by the extended Zeldovich mechanism, and the second by the N_2O mechanism.[28] The calculation of NO mass fraction requires knowledge of the mass fractions of O, H, and OH. In a previous investigation Rokke et al.[29] used the steady-state approximation for O and assumed partial equilibria for the shuffle steps $OH + H_2 \leftrightarrow H_2O + H$ and $H + O_2 \leftrightarrow OH + O$. Accordingly, we assume,

$$\tilde{\dot{m}}_{NO} = M_{NO}\bar{\rho}^2\left(A_1\tilde{\theta}^{0.3}e^{-E_1/(R\tilde{\theta})} + A_2\bar{\rho}e^{-E_2/(R\tilde{\theta})}\right)\tilde{Y}_{N_2}\tilde{Y}_{O_2} \tag{14}$$

where the pre-exponential coefficients and the activation energies for the Zeldovich and N_2O mechanisms are: $A_1 = 4.2 \times 10^9$, $E_1 = 319.6 \times 10^3$, $A_2 = 3.17 \times 10^3$, and $E_2 = 218.3 \times 10^3$, respectively.

Methods for Discretizing the Governing Equations

The governing equations are discretized on a staggered mesh by a finite volume technique. In the LES model presented, the SGS terms explicitly provided are proportional to Δ^2 and, thus, the numerical scheme adopted must be of at least third-order accuracy to avoid implicit coupling between the SGS terms and the truncation error. For evaluating the convective fluxes, we have adopted the monotonic third-order accurate SMART scheme of Gaskell and Lau.[30] This scheme is based on piecewise polynomic reconstruction of the fluxes at the control volume surfaces and strictly preserves the monotonicity of the solution by the inclusion of a flux limiter on the third-order upwind-biased interpolation approximation. For the diffusive fluxes a fourth-order accurate difference interpolation approximation has been adopted. The time advance is made with a second-order accurate Crank–Nicholson method. The discretized equations give a system in which all dependent variables are coupled; the SIMPLER scheme[31] is used to decouple velocity and pressure. Since we use the mass flux conserving transformation, the coupling between density and momentum is only through the source terms. The energy equation is updated after updating the velocity and pressure.

Simulation Object and Related Initial and Boundary Conditions

Numerical simulations of nonreacting and reacting flow have been carried out for a configuration corresponding to a flexible modular combustor with optical access.[32] On this test rig, an extensive set of data from experimental measurements, such as CARS measurements of the temperature field[33] and laser Doppler velocimetry (LDV) measurements of the velocity field[32] are available. The rig consists of a rectilinear channel, with rectangular cross section, divided into an inlet section and a combustor section equipped with a two-dimensional triangular-shaped flame holder; see Fig. 1. The fluid adopted in the simulations was assumed to be composed of

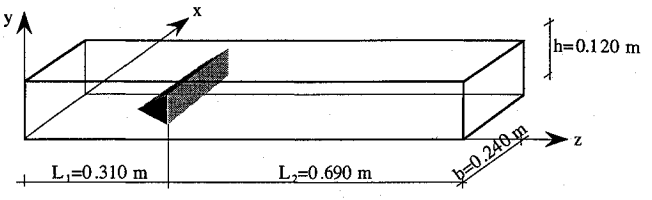

Fig. 1 Validation rig: outline, coordinate system, and overall dimensions.

79% N_2 and 21% of O_2, at atmospheric pressure. For the nonreacting case the inlet temperature was 298 K, whereas for the reacting case the inlet temperature was 600 K. In the reacting case the air was premixed with propane giving a range of equivalence ratios between $\phi = 0.50$ and $\phi = 0.90$. The mass flow rate into the combustor was allowed to vary in the range of 0.6–1.1 kg/s resulting in a Reynolds number (based on the inlet velocity on the centerline and the height of the bluff body) varying between 47,500 and 87,100 in the nonreacting case and between 24,200 and 44,300 in the reacting case.

All numerical simulations started from rest, and the unsteady flow characteristics evolved naturally. At the inlet boundary, Dirichlet conditions for the velocity, pressure, mass fractions, and enthalpy were utilized. The velocity profiles at the inlet were obtained from experimental LDV measurements[32] revealing an almost plug-shaped profile, whereas the pressure, mass fractions, and enthalpy were given uniform values across the inlet boundary. At the outflow boundary, we have followed the recommendations of Gustafsson and Sundström[34] and applied boundary conditions for all but one dependent variable. Boundary conditions for the velocity components, enthalpy, and the mass fractions are thus specified as zero Neumann conditions. For the wall boundary conditions, we followed the recommendation of Piomelli et al.,[35] whereas all remaining scalar quantities are subjected to zero Neumann conditions.

The computational grid adopted was concentrated around the bluff body, and near the channel walls, and geometrically stretched in other regions. The number of control volumes were 400 × 60 × 60, and grid refinement showed that the spatial resolution was adequate; using more control volumes showed improvement, but the difference was insignificant.

Results and Comparisons

In this section we will present results from numerical simulation in a combustion case characterized by $Re = 24{,}200$, $Ma = 0.11$, and $\phi = 0.60$. For comparison with corresponding nonreacting flow in the same test rig we refer to Fureby.[6] Experimentally measured velocity components, temperature field, rms-velocity fluctuations, rms-temperature fluctuations, and mass fractions of CO and NO are available at three cross-sections: $z = 0.348$, $z = 0.460$, and $z = 0.686$, as well as at the centerline $y = 0.060$; see Fig. 1. All measurements are made in the plane $x = 0.120$; see Refs. 32 and 33 for details.

To investigate the influence of the SGS models adopted, two simulations were performed: one relying on explicit SGS models for describing the effects of the unresolved thermo-chemical motion on the resolved motion and one without explicit SGS models, implying that the truncation error of the numerical method acts as a builtin SGS model. Monotone algorithms are designed to limit errors in the smallest resolved spatial scales in a physically meaningful way using whatever information possible. Woodward and Colella[36] and Colella and Woodward,[37] for example, indicate that monotone methods can actually be viewed as LES models with an intrinsic SGS algorithm in regions where the viscous effects cannot be resolved. In that case, this builtin SGS algorithm arises naturally from the nonlinear monotonicity preserving the flux limiting feature.

To illustrate the different behavior of nonreacting and reacting flows, instantaneous velocity fields are shown in Fig. 2. From the results of the simulations, we find that a short time interval, 0.10 s in the nonreacting case and 0.14 s in the reacting case, is required for the initial conditions to develop into a physically realistic flow. During this period there is relatively little broadening of the wake, and the vorticity seems to concentrate. Unsteady behavior is due to vortex shedding, with vortices alternatively shedding from the upper

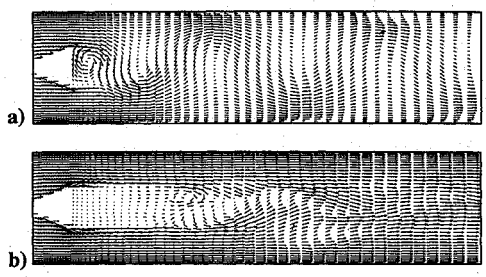

Fig. 2 Instantaneous pictures of velocity vector fields over and behind the bluff body at the centerplane $x = 0.120$: a) nonreacting case, Re = 64,000, and b) reacting case, Re = 24,200.

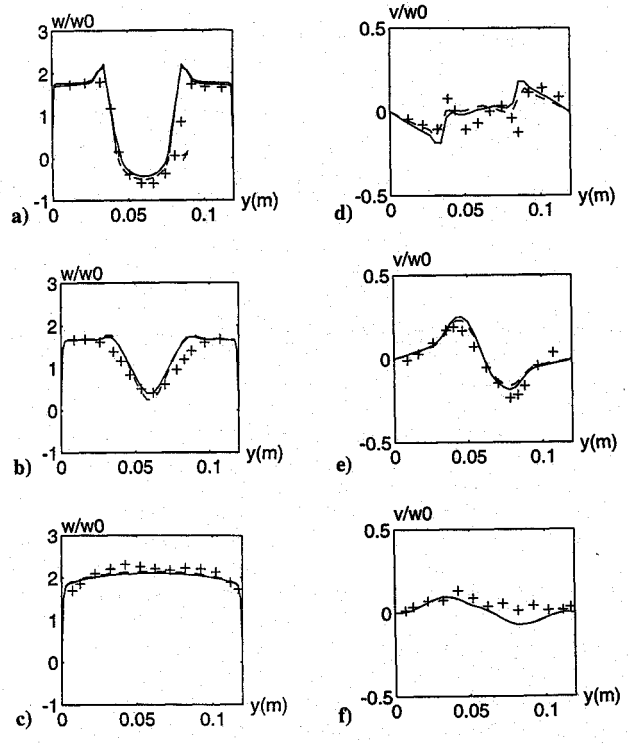

Fig. 3 Velocity profiles in three cross sections downstream of the bluff body, where + represents LDV measurements, — represents LES with SGS models, and - - - represents LES without SGS models: a) streamwise, $z = 0.348$, b) streamwise, $z = 0.460$, c) streamwise, $z = 0.686$, d) lateral, $z = 0.348$, e) lateral, $z = 0.460$, and f) lateral, $z = 0.686$.

and lower corners of the bluff body, forming a von Kármán vortex street downstream of the bluff body. In the nonreacting case, Fig. 2a, the vortex street is regular and declines gradually downstream. In the reacting case, Fig. 2b, the vortex street is significantly weaker and is initiated a small distance downstream of the almost stationary counter-rotating vortex pair residing in the primary wake zone.

The Strouhall number S based on the bluff body height and the inlet velocity was in the nonreacting case experimentally found to be $S = 0.23$, corresponding to a frequency of 102 Hz (Ref. 33); from simulations,[6] the Strouhall number was found to be $S = 0.24$. In the reacting case, the situation is somewhat different; experimentally no distinct Strouhall number is found, indicating that the vortex shedding is strongly suppressed. From the simulations presented here a large number of characteristic frequencies, having significantly lower amplitudes than in the corresponding nonreacting case, are found in the frequency range between 10 and 1500 Hz.

Figures 3–6 show ensemble-averaged quantities and corresponding rms fluctuations at three cross-sections, $z = 0.348$, $z = 0.460$, and $z = 0.686$, downstream of the flameholder. The ensemble averaging is carried out during the simulations according to: $\langle\tilde{\phi}\rangle = \Sigma_\alpha \tilde{\phi}^\alpha / N$ and the corresponding rms fluctuations are found from $\phi_{\text{rms}} = \sqrt{\langle(\tilde{\phi} - \langle\tilde{\phi}\rangle)^2\rangle} = \sqrt{\langle\phi''^2\rangle}$ where ϕ is a generic variable and N is the number of realizations or time steps used in the averaging process, typically $N = 5000$. The sampling is started after 0.2 s when the flow has developed completely.

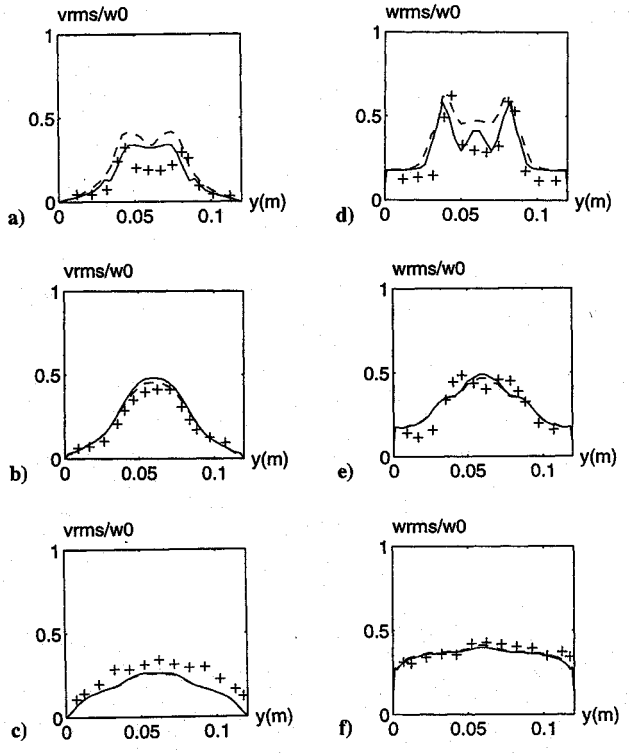

Fig. 4 Normalized rms fluctuation profiles of the velocity in three cross sections downstream of the bluff body, where + represents LDV measurements, — represents LES with SGS models, and - - - represents LES without SGS models: a) streamwise, $z = 0.348$, b) streamwise, $z = 0.460$, c) streamwise, $z = 0.686$, d) lateral, $z = 0.348$, e) lateral, $z = 0.460$, and f) lateral, $z = 0.686$.

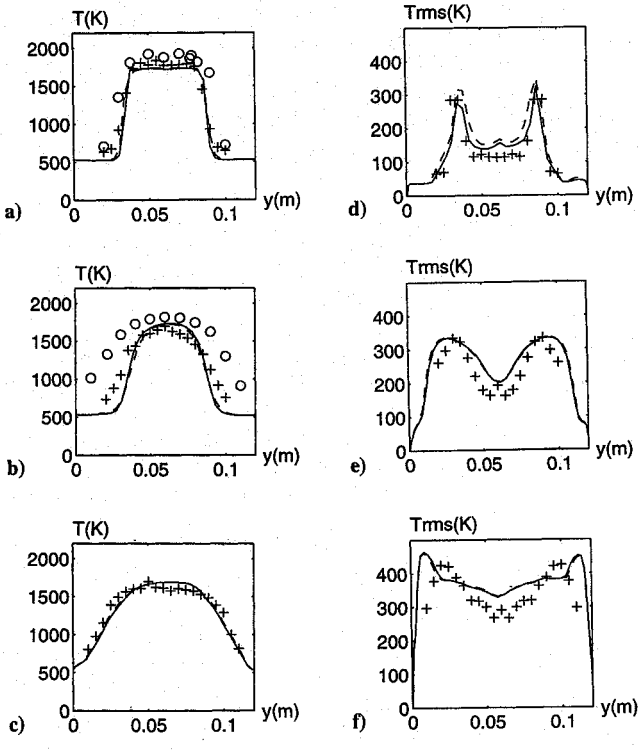

Fig. 5 Temperature profiles and corresponding rms fluctuations in cross sections downstream of the bluff body, where + represents CARS measurements, o represents gas analysis based on one-step chemistry, — represents LES with SGS models, and - - - represents LES without SGS models: a) temperature, $z = 0.348$, b) temperature, $z = 0.460$, c) temperature, $z = 0.686$, d) rms fluctuation, $z = 0.348$, e) rms fluctuation, $z = 0.460$, and f) rms fluctuation, $z = 0.686$.

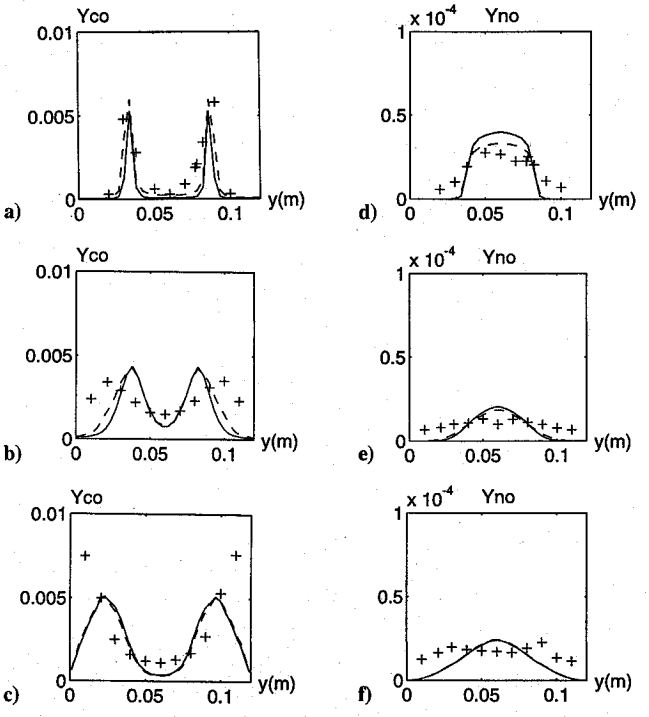

Fig. 6 Constituent mass fraction profiles, CO and NO, in three cross sections downstream of the bluff body, where + represents measurements, — represents LES with SGS models, and - - - represents LES without SGS models: a) $\tilde{Y}_{CO}$ at $z = 0.348$, b) $\tilde{Y}_{CO}$ at $z = 0.460$, c) $\tilde{Y}_{CO}$ at $z = 0.686$, d) $\tilde{Y}_{NO}$ at $z = 0.348$, e) $\tilde{Y}_{NO}$ at $z = 0.460$, and f) $\tilde{Y}_{NO}$ at $z = 0.686$.

Figure 3 shows normalized ($w_0 = 36.5$ m/s) streamwise and lateral velocity component profiles. As can be observed, the streamwise velocity profiles at all three cross sections (Figs. 3a–3c) correlate well with the measured profiles, except for the peaks in the shear layers just behind the bluff body (Fig. 3a) and that the simulated wake profile seems to be somewhat more narrow than the experimental wake profile (Fig. 3b). By comparing the streamwise velocity profiles at the centerline, it is found that the LES model underpredicts the length of the recirculation zone to a small extent (<5%) and underpredicts the magnitude of the velocity in the immediate recirculation zone (<5%); see also Fig. 3a. The lateral velocity profiles (Figs. 3d–3f) also correlate well with the measured profiles with the exception of the cross section at $z = 0.348$ (Fig. 3d). As can be observed, the influence of the SGS models on the ensemble-averaged velocity profiles are almost negligible.

The normalized ($w_0 = 36.5$ m/s) profiles of the rms fluctuation of the lateral and streamwise velocity components, corresponding to the yy and zz components of the turbulent Reynolds stresses are given in Fig. 4. Both simulations behave similarly and yield similar predictions of both rms fluctuation profiles. In general, the rms fluctuation profiles obtained from the LESs correlate well with the experimentally obtained profiles. The only significant deviation is in the lateral rms fluctuation at $z = 0.348$ (Fig. 4a) in which the shape is predicted better by the simulation without SGS models. In conclusion, the agreement between simulated and measured diagonal components of the turbulent Reynolds stress tensor is good and the idea that the LES model is capable of accurately resolving significant parts of the turbulent behavior is supported.

The temperature profiles (Figs. 5a–5c) and their corresponding rms fluctuations (Figs. 5d–5f) also show reasonable agreement with measurement data. For completeness, both CARS measured temperature profiles and temperature profiles obtained from gas analysis based on one-step chemistry[32] are shown. First, we may observe the pronounced difference between the experimental results in the two cross sections, $z = 0.348$ and $z = 0.460$ (Figs. 5a and 5b). CARS measurements are generally regarded as more reliable than gas analysis, especially in the temperature range 500–2300 K (Ref. 33); therefore, the comparisons are made primarily with the CARS measurements. Estimated error bounds for the CARS measurements are ±90 K (Ref. 33). We may, therefore, conclude that the simulations give very good agreement, both with and without the SGS models. As can be observed, the influence of the SGS models on the ensemble-averaged temperature field is almost negligible. Comparison of the rms temperature fluctuations (Figs. 5d–5f) suggests that the shape of the profiles obtained from both simulations coincide well with the measured profiles, but the magnitudes show deviations; however, they are too small to give any indications of whether SGS models are needed or not. The maximum rms fluctuations occur in two streaks originating from the upper and lower corners of the bluff body, implying that cold reactants mix with hot products in these regions.

Figure 6 shows profiles of selected mass fraction fields; Figs. 6a–6c show profiles of $\tilde{Y}_{CO}$ whereas Figs. 6d–6f show profiles of $\tilde{Y}_{NO}$. In the case of CO both simulations reproduce the measurement data with reasonable accuracy; again, hardly any difference is noticed when turning off the SGS models. The measured CO profile at $z = 0.686$ (Fig. 6c) contains two measuring points (the points close to the walls) that are not in accordance with the temperature measurement and should, therefore, be disregarded. The magnitude of the measured profiles and the magnitude of the profiles obtained from the simulations are acceptable in all cross sections indicating that the total amount of CO present at each cross section is well captured by both numerical simulations. The shape of the CO profiles is predicted differently; turning off the SGS model widens the CO profiles (Fig. 6b) slightly and improves the predictions to a small extent. In the case of NO the agreement between measured and simulated profiles is not satisfactory. At $z = 0.348$ (Fig. 6d) the profiles are too narrow, and the maximum amount of NO produced is overpredicted; in the remaining profiles (Figs. 6e and 6f) the profiles obtained from the simulations are again narrower than the experimentally obtained profiles, whereas the amplitude is slightly overpredicted. The total amount of NO present at each cross section is, however, reasonably well captured in the simulations.

Collating profiles of temperature, temperature rms fluctuations, $\tilde{Y}_{CO}$ and $\tilde{Y}_{NO}$ reveals that $\tilde{Y}_{CO}$ is formed in regions where large temperature rms fluctuations are predominant, i.e., in two streaks, characterized by strong mixing between hot products and cold reactants, originating from the upper and lower corners of the bluff body, respectively. Furthermore, $\tilde{Y}_{NO}$ is formed in the high-temperature zones that have modest fluctuation levels. As can be observed from Eq. (14) the formation of $\tilde{Y}_{NO}$ is strongly affected by the temperature; small temperature variations result in significant changes in the $\tilde{Y}_{NO}$ levels. The model used so far for NO formation lacks accurate SGS treatment, but as can be observed from (Figs. 6d–6f), this does not seem to be the cause of the discrepencies. Other causes may be that thermal radiation is predominant or that the chemical model is too simple.

In Fig. 7 a comparison of predicted and measured (using CARS) probability density functions (PDFs) of the temperature field at four

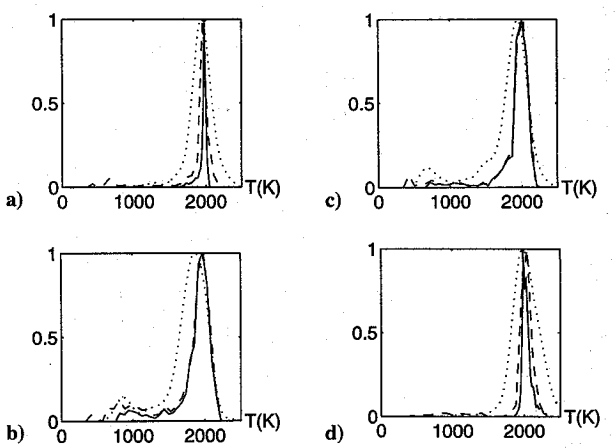

Fig. 7 Temperature probability density functions normalized with respect to their maximum values at the four positions (y, z), where measured PDFs are indicated by · · ·, simulations by —, if SGS models are turned on and by – – –, if SGS models are turned off: a) (0.080, 0.348), b) (0.080, 0.460), c) (0.080, 0.686), and d) (0.060, 0.460).

(y, z) positions, three in the shear layers (0.080, 0348), (0.080, 0.460), and (0.080, 0.686) and one at the centerline (0.060, 0.460), are presented. The simulated PDFs were obtained from a time interval of 0.2 s or 5000 samplings whereas the measured PDFs were obtained from 1000 samplings spread out over an interval of 3 min. By comparing the peaks of the measured and simulated PDFs it can be observed that the movement of the flame front is captured by the LES model and thus gives rise to PDFs, which qualitatively are similar to but narrower than the measured ones. It is further noticed that the temperature field is slightly overpredicted in some of the positions, indicating that the thermal energy removing mechanisms, conduction and radiation, might not be accurately described in the LES model.

Discussion and Interpretation of the Simulation Results

Results from the LES model described can now be used in discussing the combustion process. A similar discussion for the nonreacting flow has been carried out in Ref. 6. As indicated in Ref. 6, three-dimensional effects are important in the nonreacting flow situation and may perhaps be even more pronounced in the reacting case since the rate of chemical reactions critically depends on the small-scale three-dimensional flow. The need for a deeper understanding of the flow to evaluate different SGS models and a general interest in flame stabilization and bluff body flow motivates a discussion of the morphology of the flowfield. Results from the simulation with SGS models are used.

In Figs. 8–10 a few quantities of interest are plotted in a full height section of 0.240 m length starting at $z = 0.330$. The quantities chosen to investigate the flow characteristics are the instantaneous fluctuating velocity field ($\dot{x}' = \tilde{\dot{x}} - \langle\tilde{\dot{x}}\rangle$), the ensemble-averaged velocity field $\langle\tilde{\dot{x}}\rangle$, the baroclinic torque ($\bar{\rho}^{-1}\,\mathrm{grad}\,\bar{\rho}\times\mathrm{grad}\bar{p}$), the specific kinetic energy of the fluctuating motion ($\frac{1}{2}\dot{x}'^2$), the production of specific kinetic energy due to the fluctuating motion [$-\tau\cdot\tilde{D}$ where $\tau = \bar{\rho}(\dot{x}'\otimes\dot{x}')$], the Frobenius norm of the rate of strain tensor ($\|\tilde{D}\|$), the dissipation of specific kinetic energy of the fluctuating motion ($S'\cdot D'$ where $S' = \lambda\,\mathrm{div}\,\dot{x}' + 2\mu D'$), the normalized vortex streching ($\zeta = \tilde{\omega}\cdot\tilde{L}\tilde{\omega}/\tilde{\omega}^2$), the heat release due to chemical reactions ($\Sigma_A h^0_{Af}\bar{w}_A$), the spanwise vorticity component [$\frac{1}{2}(\mathrm{curl}\,\tilde{\dot{x}})_x$], some of the reaction rates, the thermodynamic pressure, the instantaneous temperature field, the instantaneous CO mass fraction field, and, finally, the instantaneous turbulent stresses [$\tau = \bar{\rho}(\dot{x}'\otimes\dot{x}')$].

Topologically the structure of the flow can be characterized by extremum points (centers) and saddle points denoted by + and ×, respectively. The fluctuating velocity vector field of Fig. 8a shows organized vortical motion around the centers and specifies the saddle points. In contrast to the nonreacting case in Ref. 6, the vortex shedding is not initiated directly after the bluff body but at a distance further downstream. The origin of this pronounced difference in behavior becomes evident when examining the ensemble-averaged velocity field, Fig. 8b. In the wake region, the ensemble-averaged velocity field is dominated by a pair of almost stationary counter-rotating vortices, primarily responsible for flame stabilization through recirculation of hot-combustion products. Fluctuations in the velocity or density fields induce instabilities in this vortex pair, which ultimately leads to vortex shedding. Further downstream, other processes, such as the baroclinic torque (Fig. 8c) and combined diffusion and dilatation of vorticity, become increasingly important and gradually eliminate the vortex shedding (Fig. 8d), which shows an intermittent and complex behavior.

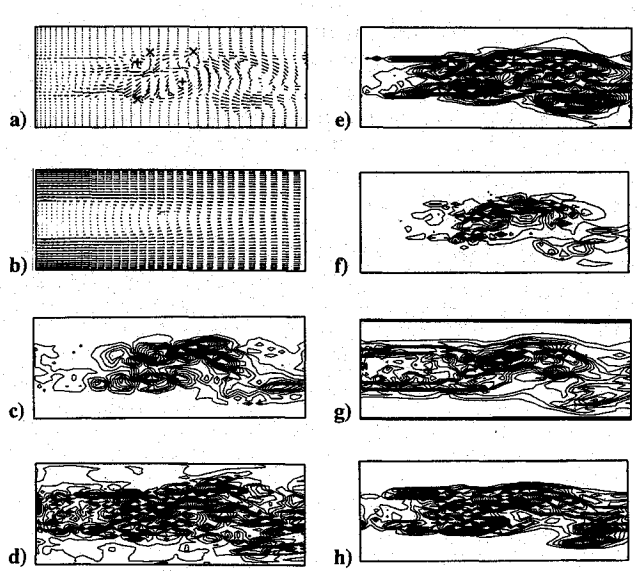

Fig. 8 Contours: a) instantaneous velocity fluctuations, b) ensemble-averaged velocity field, c) baroclinic torque, d) normalized vortex streching, e) kinetic energy of the fluctuating motion, f) production of the kinetic energy of the fluctuating motion, g) rate of strain, and h) dissipation of the kinetic energy of the fluctuating motion at the centerplane ($x = 0.120$) in a full height section of 0.24 m length starting at $z = 0.33$.

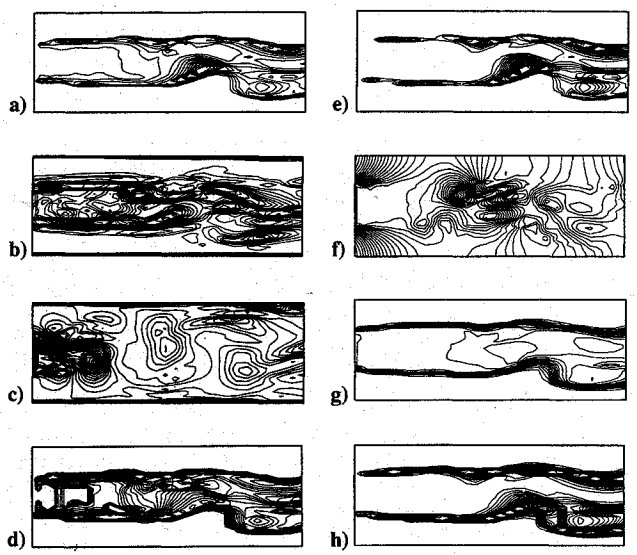

Fig. 9 Contours: a) heat release, b) spanwise vorticity component $\tilde{\omega}_x$ in the reacting case, c) spanwise vorticity component $\tilde{\omega}_x$ in the nonreacting case, d) reaction rate for the oxidation reaction $C_3H_8 + \frac{3}{2}O_2 \rightarrow 3CO + 4H_2$, e) reaction rate for the reaction $CO + \frac{1}{2}O_2 \rightarrow CO_2$, f) instantaneous pressure, g) instantaneous temperature, and h) instantaneous CO mass fraction field at the centerplane ($x = 0.120$) in a full height section of 0.24 m length starting at $z = 0.33$.

The kinetic energy of the fluctuating motion (Fig. 8e) has lower values at the front than at the back of the large-scale structures; thus, the unburnt fuel-air mixture is engulfed into the wake region primarily downstream of the structures. Further, lower contour levels at the front of the structures extend slightly toward the wake centerline implying that some fluid can be entrained from the opposite side of the wake. Furthermore, this suggests that the vortex street is not a continuous sheet but perforated. Contours of production of kinetic energy due to the fluctuating motion (Fig. 8f) and the rate of strain (Fig. 8g) are observed to have local maxima close to the saddle points. Accordingly, significant production of turbulence due to the large-scale motion occurs in the saddle regions; a similar observation was made in the nonreacting case.[6] Dissipation of kinetic energy of the fluctuating motion (Fig. 8h) occurs in a somewhat more localized fashion; peak values are predominantly localized at the front of the large-scale structures where the kinetic energy of the fluctuating motion is lower.

An important effect of the heat release from the chemical reactions (Fig. 9a) on the vorticity field (Fig. 9b) is that the vorticity field now is less structured compared with the nonreacting case[6] (Fig. 9c) and that multiple local extrema in the vorticity field have developed. Another effect of the heat release on the vorticity field is to decrease the magnitude of the vorticity field at the center of the vortex structures. The first of these two effects appears to be a result of the baroclinic torque (Fig. 8c), which also contributes in the development of a more diffuse vorticity distribution. A more diffuse vorticity field reduces the lateral velocity component and, accordingly, the straining of the

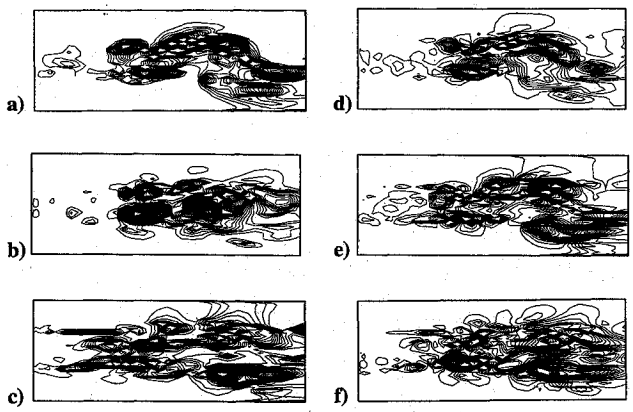

Fig. 10 Contours of the instantaneous turbulent stresses: a) normal stress component τ_{xx}, b) normal stress component τ_{yy}, c) normal stress component τ_{zz}, d) shear stress component τ_{xy}, e) shear stress component τ_{xz}, and f) shear stress component τ_{yz} at the centerplane ($x = 0.120$) in a full height section of 0.24 m length starting at $z = 0.33$.

reaction interface and the mass entrainment, which ultimately limits the rate of the chemical reactions. The second of these two effects seems to be the result of thermal expansion in the vortex cores, which is most pronounced at early times during the shedding cycle since combustion products having low density are rapidly formed in the vortex cores. Figures 9d and 9e show the reaction rates corresponding to the sequential reactions Eqs. (12a) and (12b) and Eq. (12c), respectively. From these figures the individual reaction rates are found to be intermittent and concentrated in layers with finite thickness, separating the fuel–air mixture and the combustion products. Collating the reaction rates with the heat release, it may be observed that reactions Eqs. (12a) and (12b) are less exothermic than Eq. (12c). Another important effect of heat release in reacting flows is generally to increase the viscosity and, thus, lower the Reynolds number. It can be argued that this will tend to have a stabilizing effect on the flowfield, which can be recognized if the spanwise vorticity fields of Figs. 9b and 9c are compared. The pressure field, given in Fig. 9f, shows evidence of weak pressure waves. Such pressure waves are found to have a frequency content of higher frequencies than found in the corresponding frequency content of the velocity field and, consequently, the fluid flow dynamics cannot respond to these pressure fluctuations. The instantaneous temperature field, Fig. 9g, is found to be only weakly affected by the fluctuating velocity (Fig. 8a) and the instantaneous vorticity (Fig. 9b). Hence, the dissipation $\bar{S} \cdot \bar{D}$ is negligible compared to the heat conduction and thermal radiation and, therefore, the temperature field is primarily determined by the constituent composition and the enthalpy. Since the balance equations of mass are dominated by the mass supply terms, advective and diffusive contributions are insignificant. This can be inferred, by inspecting the CO mass fraction field in Fig. 9h, which is found to be intermittent and concentrated in the shear layers.

In Fig. 10 the instantaneous turbulent stresses $\tau = \bar{\rho}(\dot{x}' \otimes \dot{x}')$ representing transport of momentum at the centerplane ($x = 0.120$) are shown. Collating the contours of the instantaneous turbulent normal stress component τ_{xx} with the fluctuating velocity field of Fig. 8a we note that the large-scale structures coincide with the extrema of τ_{xx} signifying momentum entrainment in the spanwise direction through to the large-scale structures. The fluctuating motion generates extrema in τ_{zz} above and below each vortex, with $\dot{x}_z$ positive for one extremum and negative for the other, Fig. 10c. Similarly, the alternating extrema in τ_{yy} of Fig. 10b correspond to extrema in $\dot{x}_z$. Figure 10f shows the instantaneous turbulent shear stress component τ_{yz}. This stress component exhibits antisymmetry about the wake centerline; regions of z-momentum flux toward the wake centerline are separated by smaller regions of z-momentum flux away from the centerline. In Fig. 10f we may note the large stresses associated with entrainment of freestream fluid into the regions between the large-scale structures. Another interesting feature can be observed by collating the production of turbulent kinetic energy (Fig. 8f) with τ_{yz}; we then observe that the extrema in τ_{yz} lies close to the extrema in the production and, thus, also close to the saddle points, implying that production of kinetic energy of the fluctuating motion through vortex stretching increases the turbulent shear stress.

Concluding Remarks

This paper focuses on investigating the predictive capabilities of a LES model by applying it to a well-behaved and well-documented bluff body stabilized flame configuration. Two three-dimensional numerical simulations have been performed: one relying on explicit SGS models for describing the effects of the unresolved motion on the resolved motion and one without explicit SGS models, implying that the truncation error of the numerical method acts as a builtin SGS model. From Figs. 3–6 it is obvious that both simulations predict the ensemble-averaged profiles within the error bounds of the measurements. From Fig. 7 it can furthermore be observed that the movement of the flame front is well captured by the LES model and, thus, gives rise to temperature PDFs which qualitatively are similar to the measured ones. Consequently, the method mimics most of the significant flow features, including typical unsteady flow structures.

From the results shown, it is found that the LES method is resilient to SGS modeling; in this case, the truncation error of the monotone algorithm succeed as an SGS model when the explicit SGS model is switched off. Recently, an investigation[10,11] has been initiated with the prime goal of investigating the effects of different SGS models on the resolved flowfields in greater detail. One of the most important conclusions from our combined efforts in applying LES to various flows, however, is that the cutoff wave number, associated with the particular grid, must be contained within the inertial subrange if accurate results are to be achieved. If the cutoff wave number is not contained in the inertial subrange, the results will be progressively dependent on the SGS model adopted and, in general, not as accurate as when the cutoff wave number was contained therein.

In this investigation thermal radiation and NO formation are included as separate submodels. The effects of the NO formation model is presented in Figs. 6d–6f; the model predicts the integrated amount of NO formed in the investigated cross sections fairly well but not the shape of the profiles, measurements indicate wider profiles. The reasons for this discrepancy is not yet fully understood. By switching off the thermal radiation model, the ensemble-averaged temperature increases by approximately 30 K, whereas the amount of NO increases by about 10%; in a propane flame at lean conditions, only small effects from thermal radiation on the temperature are expected.

Acknowledgments

The authors would like to thank M. Akram, E. Lundgren, and Volvo Aero Corporation for valuable discussions; National Supercomputer Centre, Linköping, Sweden, for providing the computational resources; and Concentration, Heat and Momentum, London, for providing the code Phoenics in which the LES model and the numerics are implemented.

References

[1]Deardorff, J. W., "A Numerical Study of Three-Dimensional Turbulent Channel Flow at Large Reynolds Numbers," *Journal of Fluid Mechanics*, Vol. 41, No. 2, 1970, pp. 453–478.

[2]Kim, J., and Moin, P., "Large Eddy Simulation of Turbulent Channel Flow," AGARD Symposium on Turbulent Boundary Conditions, The Hague, 1979.

[3]Ferziger, J. H., and Leslie, D. C., "Large Eddy Simulation—A Predictive Approach to Turbulent Flow Computation," AIAA Paper 79-1441, 1979.

[4]Zang, T. A., Dahlburg, R. B., and Dahlburg, J. P., "Direct and Large-Eddy Simulations of Three-Dimensional Compressible Navier–Stokes Turbulence," *Physics of Fluids A*, Vol. 4, No. 1, 1992, pp. 127–140.

[5]Speziale, C. G., Erlbacher, G., Zang, T. A., and Hussaini, M. Y., "The Subgrid-scale Modelling of Compressible Turbulence," *Physics of Fluids A*, Vol. 31, No. 4, 1988, pp. 940–942.

[6]Fureby, C., "Large Eddy Simulations of Turbulent Anisochoric Flows," *AIAA Journal*, Vol. 33, No. 7, 1995, pp. 1263–1272.

[7]Menon, S., and Jou, W.-H., "Large-Eddy Simulations of Combustion Instability in an Axisymmetric Ramjet Combustor," *Combustion Science and Technology*, Vol. 75, Nos. 1–3, 1991, pp. 53–72.

[8]Fureby, C., and Löfström, C., "Large-Eddy Simulations of Bluff Body Stabilized Flames," *25th Symposium (International) on Combustion*, Combustion Inst., Pittsburgh, PA, 1994, pp. 1257–1264.

[9]Frankel, S. H., Adumitroaie, V., Madnia, C. K., and Givi, P., "Large Eddy Simulation of Turbulent Reactive Flows by Assumed Pdf Methods," *Engineering Applications of LES*, FED-Vol. 162, American Society of Mechanical Engineers, New York, 1993, pp. 81–101.

[10]Fureby, C., "On Sub Grid Scale Modeling in Large Eddy Simulations of Compressible Fluid Flow," *Physics of Fluids A*, 1995 (submitted for publication).

[11]Fureby, C., "On Reaction Rate Modeling in Large Eddy Simulations of Chemically Reacting Flows," *Physics of Fluids A*, 1995 (submitted for publication).

[12]Truesdell, C., *Rational Thermodynamics*, Springer–Verlag, Berlin, 1984, Chap. 5.

[13]Fureby, C., Lundgren, E., and Möller, S.-I., "Mixture Models for Combustion," *Progress in Energy, Combustion, and Science*, 1995 (submitted for publication).

[14]Leslie, D. C., and Quarini, G. L., "The Application of Turbulence Theory to the Formulation of Sub-Grid Modeling Procedures," *Journal of Fluid Mechanics*, Vol. 91, No. 1, 1979, pp. 65–91.

[15]Piomelli, U., Cabot, W. H., Moin, P., and Lee, S., "Subgrid Scale Backscatter in Turbulent and Transitional Flows," *Physics of Fluids A*, Vol. 3, No. 7, 1991, pp. 1766–1771.

[16]Chasnov, J. R., "Simulation of the Kolmogorov Inertial Subrange Using an Improved Subgrid Model," *Physics of Fluids A*, Vol. 3, No. 1, 1991, pp. 188–200.

[17]Leith, C. E., "Stochastic Backscatter in a Sub-grid Scale Model: Plane Shear Mixing Layer," *Physics of Fluids A*, Vol. 2, No. 3, 1990, pp. 297–299.

[18]Leonard, A., "Energy Cascade in Large-Eddy Simulation of Turbulent Fluid Flows," *Advances in Geophysics*, Vol. 18A, 1974, pp. 237–248.

[19]Bardina, J., Ferziger, J. H., and Reynolds, W. C., "Improved Turbulence Models based on Large-Eddy Simulation of Homogeneous, Incompressible Turbulent Flows," Dept. of Mechanical Engineering, Stanford Univ., Rept. TF-19, Stanford, CA, 1983.

[20]Menon, S., "A Numerical Study of Secondary Fuel Injection Control of Combustion Instability in a Ramjet," AIAA Paper 92-0777, 1992.

[21]Kuo, A. Y., and Corrsin, S., "Experiments on Internal Intermittency and Fine Structure Distribution Functions in Fully Turbulent Fluid," *Journal of Fluid Mechanics*, Vol. 50, Nov. 1971, pp. 285–319.

[22]Kuo, A. Y., and Corrsin, S., "Experiment on the Geometry of the Fine-Structure Regions in Fully Developed Turbulent Fluid," *Journal of Fluid Mechanics*, Vol. 56, Dec. 1972, pp. 447–479.

[23]Magnussen, B., "On the Structure of Turbulence and a Generalized Eddy Dissipation Concept for Chemical Reaction in Turbulent Flow," 19th AIAA Aerospace Science Meeting, St. Louis, MO, 1991.

[24]Hautman, D. J., Dryer, F. L., Schug, K. P., and Glassmann, I., "A Multi-step Overall Kinetic Mechanism for Oxidation of Hydrocarbons," *Combustion Science and Technology*, Vol. 25, Nos. 5, 6, 1981, pp. 219–235.

[25]Bowman, C. T., "Kinetics of Polutant Formation and Destruction in Combustion," *Progress in Energy Combustion and Science*, Vol. 1, 1975, pp. 33–45.

[26]Miller, J. A., and Bowman, C. T., "Mechanism and Modeling of Nitrogen Chemistry in Combustion," *Progress in Energy Combustion and Science*, Vol. 15, 1989, p. 287.

[27]Drake, M. G., and Blindt, R. J., "Calculation of NO_x Formation Pathways in Propagating Laminar, High Pressure Premixed CH_4/Air Flames," *Combustion Science and Technology*, Vol. 75, Nos. 4–6, 1991, pp. 261–285.

[28]Malte, P. C., and Pratt, D. T., "The Role of Energy-Releasing Kinetics in NO_x Formation: Fuel-Lean, Jet Stirred CO-Air Combustion," *Combustion Science and Technology*, Vol. 9, Nos. 5, 6, 1974, pp. 221–231.

[29]Rokke, N. A., Hustad, J. E., Sonju, O. K., and Williams, F. A., "Scaling of Nitric Oxide Emissions from Buoyancy Dominated Hydrocarbon Jet Diffusion Flame," *24th Symposium (International) on Combustion*, Combustion Inst., Pittsburgh, PA, 1992, pp. 385–393.

[30]Gaskell, P. H., and Lau, A. K. C., "Curvature-compensated Convective Transport: SMART, A new Boundedness-preserving Transport Algorithm," *International Journal of Numerical Methods in Fluids*, Vol. 8, 1988, pp. 617–641.

[31]Patankar, S. V., and Spalding, D. B., "A Calculation Procedure of Heat, Mass and Momentum Transfer in Three Dimensional Parabolic Flows," *International Journal of Heat and Mass Transfer*, Vol. 15, 1980, pp. 1787–1805.

[32]Sjunneson, A., Olovsson, S., and Sjöblom, B., "Validation Rig—A Tool for Flame Studies," Volvo Aero Corp., S-461 81, Trollhättan, Sweden, Aug. 1991.

[33]Sjunnesson, A., Henriksson, P., and Löfström, C., "Cars Measurements and Visualization of Reacting Flows in a Bluff Body Stabilized Flame," AIAA Paper 92-3650, 1992.

[34]Gustafsson, B., and Sundström, A., "Incompletely Parabolic Problems in Fluid Dynamics," *Journal of Applied Mathematics*, Vol. 35, No. 2, 1978, pp. 343–357.

[35]Piomelli, U., Ferziger, J. H., Moin, P., and Kim, J., "New Approximate Boundary Conditions for Large Eddy Simulations of Wall-bounded Flows," *Physics of Fluids A*, Vol. 1, No. 6, 1989, pp. 1061–1068.

[36]Woodward, P., and Colella, P., "The Numerical Simulation of Two-dimensional Fluid Flow with Strong Shocks," *Journal of Computational Physics*, Vol. 54, No. 1, 1984, pp. 115–173.

[37]Colella, P., and Woodward, P., "The Piecewise Parabolic Method (PPM) for Gas Dynamic Simulations," *Journal of Computational Physics*, Vol. 54, No. 1, 1984, pp. 174–201.